CME LIVE OPEN ACCESS

Journal of
Petroleum Gas & Chemical Engineering

Research Article

Computational Analysis of the Impacts of Inner Obstacles and Periodic Heating on Heat Transfer for Natural Convection Fluid Flow Inside a Square Chamber

Ashikur Rahman, Sadia Islam, Rukaya Parven and Md Aslam Hossain*

Department of Mathematics, Pabna University of Science and Technology, Pabna-6600, Bangladesh.

***Correspond Author:** Md Aslam Hossain, Department of Mathematics, Pabna University of Science and Technology, Pabna-6600, Bangladesh.

Received: 2024 Nov 24 **Accepted:** 2024 Dec 13 **Published:** 2024 Dec 22

Abstract

The results of this research have wide-ranging engineering and industrial implications, especially in the areas of electronic cooling, industrial heat exchangers, energyefficient building design, and thermal management system optimization. The results advance energy storage technology, improve thermal insulation techniques, and improve HVAC system performance. The findings are also useful for microfluidic devices and aerodynamic design, whenever appropriate regulation of fluid flow as well as warmth exchange is crucial for dependability and efficiency. The finite element Galerkin residual method is used to examine transmission of heat properties and natural convection circulate movement in a square cavity with an inside insulated rectangular obstruction. The cavity's right boundary is maintained at a steady cold the outside temperature, the upper layer is adiabatic and the inner walls of the obstacles are kept adiabatic in one case and heated in another case, and the left and bottom walls are heated unevenly. With COMSOL Multiphysics, the Boussinesq approximationbased governing equations for steady-state natural convection (NC) are numerically resolved. To guarantee the accuracy of the solution, a grid independence test is performed. For Ra ranging from 10^3 to 10^6, the impacts of Rayleigh number (Ra) on velocity, isotherm contours, and Nusselt number distribution are examined. "Lastly, a Comparison between the adiabatic obstacle and heated obstacle on heat transfer rate are presented graphically." The findings indicate that raising Ra promotes convective motion, which causes heat transfer to move from regimes dominated by conduction to those dominated by convection. Ra considerably raises maximum velocity, and temperature gradients close to heated and cooled walls get steeper. As Ra increases, the Nusselt number distribution shows better convective heat transmission, especially at the bottom and left heated walls.

Keywords: Square Cavity, Rectangular Block, Natural Convection, Rayleigh Number, Nusselt Number

1. Introduction

In view of its simplicity and uses in solar energy systems, nuclear energy, materials processing, electronics cooling, and food sterilization, natural convection in air-filled square cavities is crucial. Free convection (FC) within the cavity has been used in many real-world applications over the past few decades, such as the semiconductor industry, solar panels radiation enthusiasts, technological system cooling purposes, etc. [1,2]. Convective heat transfer has emerged as a crucial area of focus for thermal management and efficiency optimization in some engineering specialties. Increasing the contact region within the liquids and solid material surfaces, altering the working fluid's quantity movement speed, using a material with a high thermal conductivity, and other methods are some ways to promote heat transfer [3,4]. several geometrical characteristics, such as an enclosure's inclination angle, Rayleigh number, and heat source position, have been used in several studies to intensify convective heat transfer [5-7].

Adding nanoparticles is a new technique that has emerged with the rapid growth of nanotechnology and can increase the rate of heat transmission [8,9]. But in some real-world uses (like crystal growth), an external magnetic field can greatly reduce natural convection and heat transfer, which helps regulate the quality of the crystal during semi-conductor crystal growth [10,11]. The immersive process of NC creates intricacy in further knowledge of the circulation fields configuration and the transfer of warmth characteristics of the interior under the age of the magnetic field (MF) influence because of the intricate collaboration of flow and magnetic fields. In many fields of applied research, the relationship between flow and MF, or magnetohydrodynamics (MHD), has been receiving a lot of attention. used numerical models to look into the impact of an applied MF on crystal formation at the beginning of 1980 [12]. They showed that the MF slowed down NC flow in addition to the power of the MF appeared to have an impact on crystal formation. In order to investigate a two-dimensional cavity's free convective flow in the presence of a transverse MF, developed mathematical formulas [13]. They demonstrated that the temperature and

velocity distributions within a central section obeyed the concept of influence of the Ha number. The flow circulation close to an enclosure's vertical walls is investigated using a global approximation function that involves a series expansion. A numerical study of MHD free convection within an equilateral vessel with a fluid that conducts electricity and a MF parallel to gravity was conducted by [14].

Convection dominates in the middle of a rectangular enclosure when the *Ha* number and Grashof number are low and high, resulting in the predominance of vertical temperature stratification. The impact of a MF event that occurred towards the left side or right turn down corner of a heating or cold wall on MHD condensation in a rectangular piece hollow was recently investigated by [15]. The consequences of the inclined position are an intriguing subject in broader scenarios where what occurred MF is angled toward the wall of the cage. The procedure of the flow-magnetic environment communication is made much becomes detailed by the existence of magnetic tilt, which causes MHD convective flow with variation of Lorentz force in addition to the movement of the constant field of electricity that is either parallel to or perpendicular to gravity [16,17]. The general conclusions can be summed up as follows: in a chamber that experiences heating variously, the buoyant flow field will be impacted by the inclined magnetic field, which will cause a difference in the rate of transmitting heat. For example, employed the limited amount approach in terms of numbers investigate MHD condensation in a box full with water underneath varying MF angles that take the shape of streamlines, components of speed, and isotherms for various operating parameter combinations [18].

They showed that flow structure and hence the properties of heat transport are significantly impacted by the direction of the applied magnetic field. Examined the NC circulation for shifts up to 135 degrees in a boxy container under the governing equations by numerically solving them. 0 degrees, 45 degrees, and 90 degrees magnetic inclination angles [19]. They demonstrated that streamlines and isotherms were significantly impacted by in two ways the placement of the barrier or the MF direction. The temperature distribution was impacted and several eddies were produced by an enclosure with a counterclockwise tilt. Multifaceted MHD condensation flows in an oblong area under perpendicular conditions: a numerical analysis of MF angles was conducted by [10]. They revealed ensure motion field and the transport warmth performance are drastically impacted by the enclosure aspect ratio and the location of the MF. Additionally, they initially noticed that the change in magnetic inclination angles caused both duality and singular heat modes transmission rate. In an earlier time, work, used numerical analysis to examine how the Lorentz force affected heat transfer (HT) and NC flow in a distorted cubical vessel or box exposed to a MF [20,21]. Based on the temperature and iso-surface distributions, the petition MF has a substantial impact heating up transmission mode. In order to examine the MHD flow arrangement and the HT characteristic beyond the barrier, streamline contours and isotherms are always depicted from a literature survey.

However, there hasn't been a thorough investigation of how the HT rate varies at different magnetic inclination (MI) angles yet, especially when it comes to the key condition for the heat transfer pattern flipping. A comprehensive algorithmic evaluation of different MI angles from θ = 0degto180deg is therefore the goal of the current study, with special focus to the convective HT design within a squared enclosing. To determine which HT pattern is dominated either the force of Lorentz or dynamically buoyed flows produced by the MF, special attention is paid to the convective HT transition. In order to improve comprehension of the HT mechanism and aid in the optimal architecture of connected MHD technologies and frameworks, the closely associated forecasts of HT transition are finally put forth. Natural convection and heat transmission in diverse enclosures and situations have been the subject of several investigations. The Ra has a major impact on flow profiles and HT, with conduction predominating at low Rayleigh numbers, as demonstrated by [22]. According to Parvin and Nasrin flow and temperature fields in MHD free convection are influenced by a circular body's size as well as its Rayleigh number [23]. Showed that fluid flow and Nusselt number in a round permeable box are affected by the size and presence of a circular block [24]. A Heat-transferable square bodies impact on HT across a vertical space is contingent upon its thermal conductivity ratio, as demonstrated by [25]. According to Larger aspect ratios of heated plates and higher Grashof values result in increased heat transfer rates [26]. According to heat transfer rises with increasing Rayleigh numbers but falls with bigger block aspect ratios at low Rayleigh numbers [27].

According to cylinder location and Richardson numbers affect the stream and temporal variations in a square space [28]. Found that the Grashof number, wall inclination angle, and nanoparticle characteristics affect movement of liquids in a polygonal vessel filled with nanofluid [29]. According to Sidewall inclination effects decrease as Rayleigh numbers rise, improving the average Nusselt number [30]. According to Roy and Basak HT is greatest at the cores of barriers and least at their edges when heating is not uniform [31]. The quantity of blocks has a major impact on flow and heat areas in a barrier propelled by a double lid, as shown by [32]. In a lid-driven cavity, demonstrated how heater dimensions affect natural convection, with higher Hartmann numbers expanding the thermal boundary layer [33]. Low Darcy numbers produce smooth, parallel heatlines throughout a range of Grashof, Prandtl, and Reynolds numbers, according to [34]. Discovered that magnetic field intensity (Ha) changes flow patterns but has little effect on thermal currents [35]. Higher Eckert numbers (Ec) have been shown by to increase temperature, velocity, and frictional force at the wall while decreasing heat transfer rates [36]. Skin friction (SF) and HT are more significantly impacted than speed and the climate. The thermal performance of a TiO2–water into small-molecule fluid in a zigzag hollow was conducted by with an emphasis on mixed convection with and without heated barriers [37]. How heat transport is affected by magnetic fields in a hollow with a heated bottom that is wavy were examined by [38]. In summary, mixed convection improves HT in nanofluid-filled spaces; important variables are cavity

inclination, Ra, volume fraction, nanoparticle size, and heat source the status of.

2. Physical Model

A symmetrical aperture conceptual illustration with an external measurement of one meter and an internal rectangular obstacle is shown in Figure 1. The cavity's bottom barrier and left barrier are heated non-uniformly, according to a temperature distribution, whereas the high wall on the other side is kept at a constant cold temperature. The top wall and all of the internal rectangular obstacle's walls, which have dimensions l = 0.3*m* and *h* = 0.1*m*, are adiabatic; all of the walls are in a no-slip condition, which means that there is no relative motion between the fluid and the boundary; the reference pressure is set to zero. This configuration is frequently used in heat transfer and computational fluid dynamics (CFD) studies to examine thermal behavior and flow characteristics within an enclosed space that contains an insulated object.

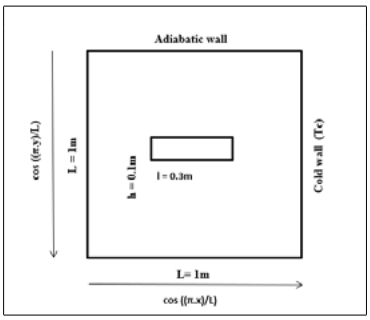

Figure 1: Square Aperture Illustration

3. Governing Equations and Boundary Conditions

The governing equations for steady NC flow, considering the Boussinesq approximation, are predicated on the ideas of mass, motion, and energy conservation.

Continuity Equation (Mass Conservation)

$$\frac{\partial u}{\partial x}+\frac{\partial v}{\partial y}=0 \tag{1}$$

Momentum Equations

X-Momentum Equation

$$u\frac{\partial u}{\partial x}+v\frac{\partial u}{\partial y}=-\frac{1}{\rho}\frac{\partial P}{\partial x}+\nu\left(\frac{\partial^2 u}{\partial x^2}+\frac{\partial^2 u}{\partial y^2}\right) \tag{2}$$

Y-Momentum Equation

$$u\frac{\partial v}{\partial x}+v\frac{\partial v}{\partial y}=-\frac{1}{\rho}\frac{\partial P}{\partial y}+\nu\left(\frac{\partial^2 v}{\partial x^2}+\frac{\partial^2 v}{\partial y^2}\right)+g\beta(T-T_c) \tag{3}$$

Energy Equation

$$u\frac{\partial T}{\partial x}+v\frac{\partial T}{\partial y}=\alpha\left(\frac{\partial^2 T}{\partial x^2}+\frac{\partial^2 T}{\partial y^2}\right) \tag{4}$$

Boundary Conditions

Boundary conditions that were applied to the square cavity are

Velocity Boundary Conditions (No-Slip Condition)

$$u(x,0)=u(x,L)=u(0,Y)=u(L,y)=0$$

$$v(x,0)=v(x,L)=v(0,y)=v(L,y)=0$$

Temperature Boundary Conditions

Bottom Wall

$$T(x,0)=(T_h-T_c)\cos\left(\frac{\pi x}{L}\right)+T_c \tag{7}$$

Top Wall (Insulated)

$$\frac{\partial T}{\partial y}(x,L)=0 \tag{8}$$

Left Wall

$$T(0,y)=(T_h-T_c)\cos\left(\frac{\pi y}{L}\right)+T_c \tag{9}$$

Right Wall

$$T(L,y)=T_c \tag{10}$$

On the walls of block (For Heated Inner Wall):

$$T=T_h \tag{11}$$

x and *y* represent the locations obtained along the horizontal and vertical axes, respectively; *u and v represent the velocity components in the x- and y- directions; P and ρ represent the pressure and density*, respectively; T_h and T_c represent the temperatures at the hot and cold walls; and *L* represents the side of the square cavity.

Dimensional Analysis (Non-Dimensional Variables)
Those that follow without dimensions objects are set up.

Non-Dimensional Coordinates

$$X = \frac{x}{L}, \quad Y = \frac{y}{L} \tag{12}$$

Non-Dimensional Velocity Components

$$U = \frac{uL}{\alpha}, \quad V = \frac{vL}{\alpha} \tag{13}$$

Non-Dimensional Pressure

$$P = \frac{PL^2}{\rho\alpha^2} \tag{14}$$

Non-Dimensional Temperature

$$\theta = \frac{T - T_c}{T_h - T_c} \tag{15}$$

Using these transformations, the temperature can be expressed as:

$$\frac{\partial U}{\partial X} + \frac{\partial V}{\partial Y} = 0 \tag{16}$$

$$U\frac{\partial U}{\partial X} + V\frac{\partial U}{\partial Y} = -\frac{\partial P}{\partial X} + Pr\left(\frac{\partial^2 U}{\partial X^2} + \frac{\partial^2 U}{\partial Y^2}\right) \tag{17}$$

$$U\frac{\partial V}{\partial X} + V\frac{\partial V}{\partial Y} = -\frac{\partial P}{\partial Y} + Pr\left(\frac{\partial^2 V}{\partial X^2} + \frac{\partial^2 V}{\partial Y^2}\right) + RaPr\theta \tag{18}$$

$$U\frac{\partial \theta}{\partial X} + V\frac{\partial \theta}{\partial Y} = \frac{\partial^2 \theta}{\partial X^2} + \frac{\partial^2 \theta}{\partial Y^2} \tag{19}$$

The following are the parameters in the previous equations:

$$Pr = \frac{\nu}{\alpha}, \quad Ra = \frac{g\alpha(T_h - T_c)L^3}{\nu * k}, \quad and \quad \alpha = \beta = k = 1. \tag{20}$$

The following are the modified non-dimensional boundary conditions (b.c.).

$$U(X,0) = U(X,L) = U(0,Y) = U(L,Y) = 0 \tag{21}$$

$$V(X,0) = V(X,L) = V(0,Y) = V(L,Y) = 0 \tag{22}$$

$$\theta(X,0) = \cos(\pi X), \quad \frac{\partial \theta}{\partial Y}(X,L) = 0 \tag{23}$$

$$\theta(0,Y) = \cos(\pi Y), \quad \theta(L,Y) = 0 \tag{24}$$

In this instance, *X* and *Y* represent dimensionless coordinates that vary in both horizontal and vertical directions, respectively; *U* and *V* represent dimensionless velocity components in the *X* and *Y* directions; θ represents the dimensionless temperature; *P* represents the dimensionless pressure; and Ra and Pr represent the Rayleigh and Prandtl numbers, respectively. The *HT* rate in terms of average Nusselt number (*Nu*) is defined by.

$$N_u = -\frac{\partial \theta}{\partial n} \tag{25}$$

here n denoted the normal direction on a plane.

4. Methodology

The finite element Galerkin method is used to numerically solve the governing non-dimensional equations and the boundary conditions. A detailed procedure of the solution technique explained by [39]. The whole fluid domain is separated into non-overlapping triangular-shaped components in order to assess the temperature and velocity profile. The convergence criterion is set as.

$$|\eta^{n+1} - \eta^n| \leq 10^{-5} \tag{26}$$

where η (*U, V,* θ) indicates the value of the iterations and *n* + 1 and *n* are two consecutive iterations. The inquiry has been simulated using COMSOL Multiphysics, a computational tool based on the finite element method. In order to compare the governing equations with the built-in vector equations in COMSOL, the dimensionless parameters are first used to convert the governing equations into dimensionless form. By evaluating the formulae, the variable values selected in way so that the integrated formulas in COMSOL depict the formulas that need to be completed.

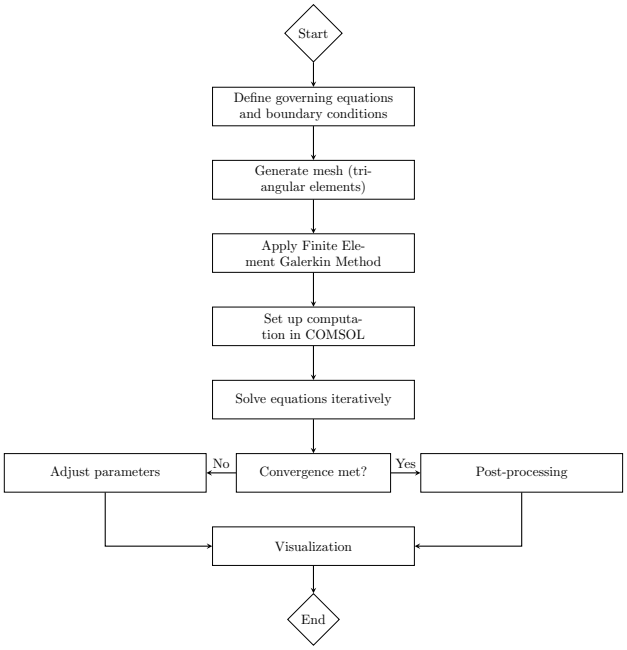

Figure 2: Methodology Flowchart

5. Grid Independent Test and Mesh Generation

We calculate the Nusselt number for Pr = 0.71 and Re = 100 to confirm the mesh independence of the numerical solution, and the outcomes are tabulated. The free triangular element of extra

Mesh Size	No. of Elements (Domain)	No. of Elements (Boundary)	Nusselt Number	Computation Time
GS-1	2678	170	3.7380	6 s
GS-2	4192	212	3.7449	7 s
GS-3	10424	426	3.7653	12 s
GS-4	26286	816	3.7743	23 s
GS-5	34598	816	3.7746	29 s

Table 1: Calculation of Nusselt Number of Grid Independent Test for Ra = 10^5

Fine size is chosen for mesh generation.

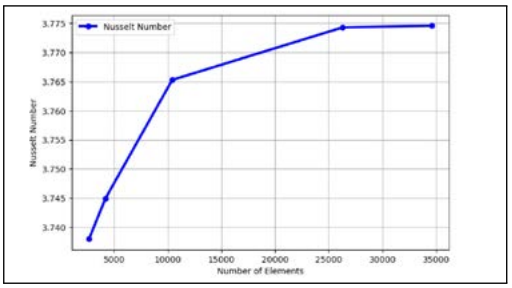

Figure 3: Grid Independent Test

Figure 4 shows the mesh generation of the above problem. The mesh consists of 26286 domain elements and 816 boundary elements. The number of degrees of freedom solved for is 57436. It takes 23 seconds for computing the value.

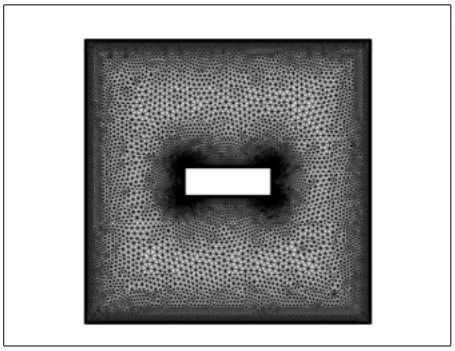

Figure 4: Mesh Generation

6. Model Validation

The accuracy of the code is confirmed by Figure 5, which displays a strong match between the streamlines and isotherms from the current numerical models as well as the ones that [38]. The outcomes of are displayed in the top row, while the results of the current investigation are displayed in the bottom row, emphasizing their similarities [38]. The average Nusselt numbers (Nu_{av}) for various widths (W) and Richardson numbers (R_i) are shown in Table 2, which contrasts the current findings with those of [38]. The strong agreement between the two datasets attests to the numerical model's dependability for researching fluid flow dynamics and heat transfer.

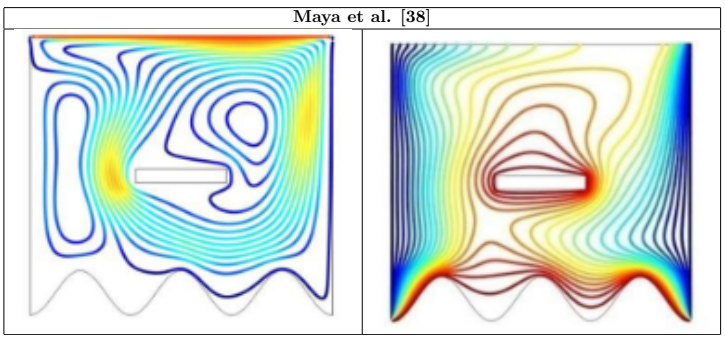

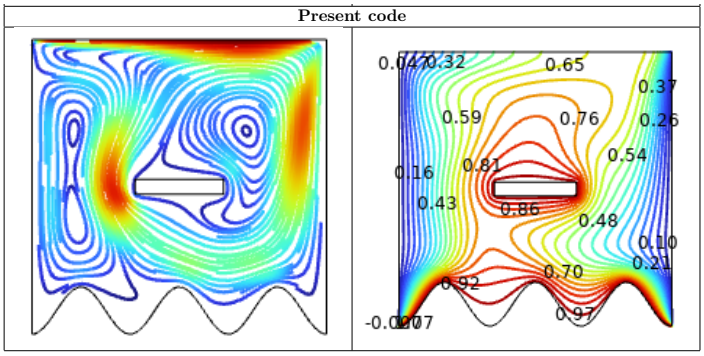

Figure 5: Parallelism of Streamlines and Isotherms as Determined by with the Present Code at *Pr* = 0.7, *Ri* = 5, *Ha* = 0

Ri	W = 0.30		W = 0.40		W = 0.45	
	Maya et al. [38]	Present code	Maya et al. [38]	Present code	Maya et al. [38]	Present code
0.1	6.8779	6.7010	6.722	6.5485	6.646	6.4784
1	7.2556	7.0688	7.0542	6.8656	6.9359	6.7531
5	7.9478	7.7625	7.7845	7.5869	7.6856	7.4873
10	8.6039	8.4098	8.4542	8.2448	8.3033	8.1034

Table 2: Average Nusselt Numbers (Nu)

7. Results and Discussions

7.1 Effects of Rayleigh Number on Streamline (Non-Heated Inner Hall)

The streamline plots for NC within a four-sided hole at Rayleigh numbers (*Ra*) ranging from 10^3 to 10^6 are displayed in Figures 6 to 9. The flow gets stronger and more intricate as Ra rises. When vortices move from the center to the corners, the maximum velocity increases from 2.75 m/s at *Ra* = 10^3 to 248 m/s at *Ra* = 10^6. Maximum velocities are shown by red contours, and minimum velocities are shown by green contours.

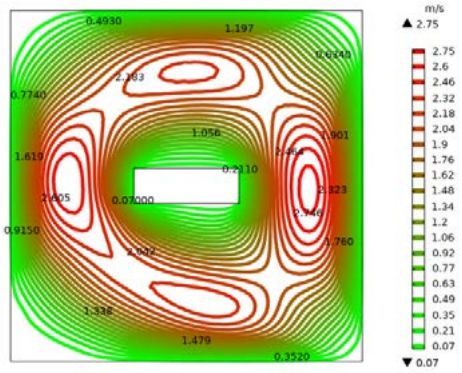

Figure 6: Streamline for *Ra* = 10^3

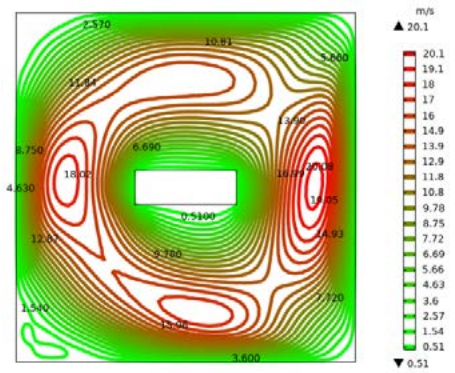

Figure 7: Streamline for *Ra* = 10^4

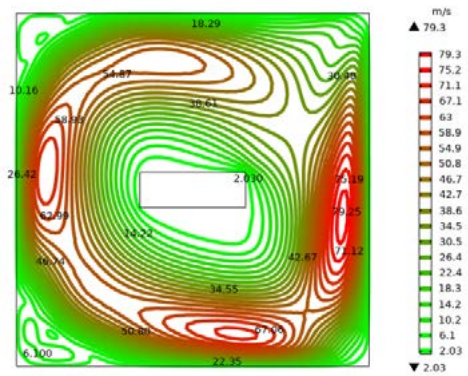

Figure 8: Streamline for *Ra* = 10^5

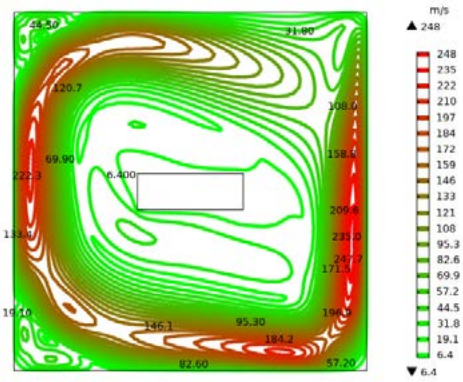

Figure 9: Streamline for *Ra* = 10^6

7.2 Effects of Rayleigh Number on Streamline (Heated Inner Wall)

The fluid flow behavior for various Rayleigh numbers (*Ra*) is depicted by the set of streamline plots in Figures 10 to 13. Stronger convection is shown by a more complex flow pattern as the Rayleigh number rises from 10^3 to 10^6. The streamlines in (Ra = 10^3 and 10^4) are symmetrical and quite smooth, with a primary circulation developing around the center blockage. The flow displays more complex vortex structures in (*Ra* = 10^5 and 10^6), with stronger velocity gradients close to the boundaries. Higher Rayleigh numbers indicate a greater velocity, especially close to the vertical borders and around the obstruction. The color shift from green to red shows the degree of velocity. Together, these figures show how, as the Rayleigh number rises, conduction dominated flow gives way to convection-dominated flow.

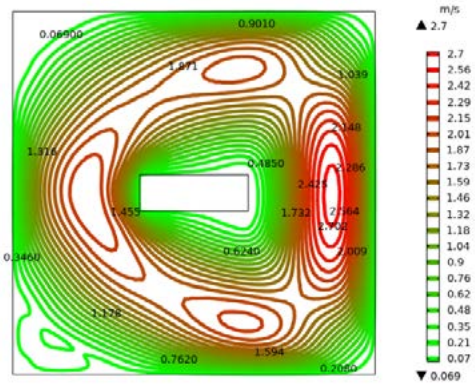

Figure 10: Streamline for *Ra* = 10^3

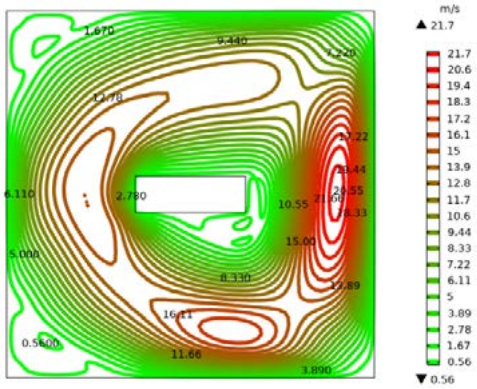

Figure 11: Streamline for *Ra* = 10^4

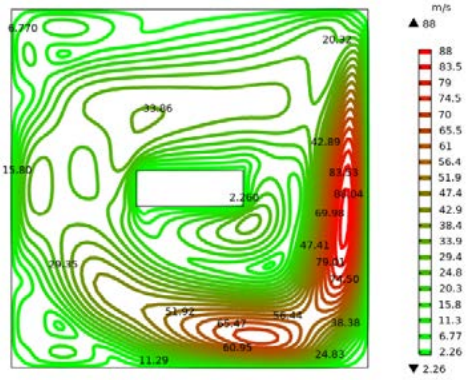

Figure 12: Streamline for *Ra* = 10^5

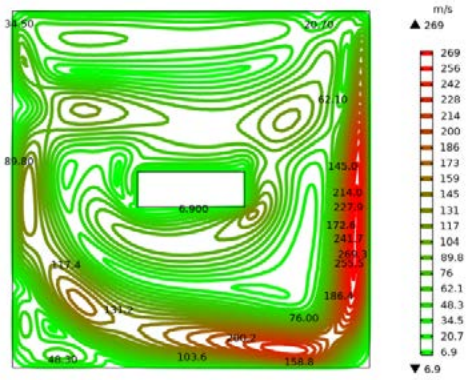

Figure 13: Streamline for *Ra* = 10^6

7.3 Effects of Rayleigh Number on Isotherm Contours (Non-Heated Inner Wall)

The isotherm contours for various Rayleigh numbers (*Ra*) within a square domain with a rectangular obstacle are shown in Figures 14 to 17. As Ra rises, the temperature distribution is represented by the isotherms, which demonstrate the change convection-dominated heating opposed to conduction-dominated heating transmission. The isotherms in (*Ra* = 10^3) are almost parallel, suggesting a strong conduction mode with negligible convection effects. The isotherms begin to bend, indicating the onset of convective heat transfer, as seen in (*Ra* = 10^4). The isotherm lines become significantly curved at *Ra* = 10^5, generating heat plumes and signifying increased convective circulation surrounding the blockage. Lastly, the isotherms in (*Ra* = 10^6) exhibit notable distortions, with tight spacing close to the walls and more intricate flow patterns, emphasizing a strongly convective regime with enhanced thermal mixing. The effect of buoyancy-driven flow is highlighted by the rising non-linearity of the isotherms across these figures, which go from a steady conductive state to an active convective state as *Ra* rises.

Citation: Rahman, A., Islam, S., Parven, R., Hossain, A. (2024). Computational Analysis of the Impacts of Inner Obstacles and Periodic Heating on Heat Transfer for Natural Convection Fluid Flow Inside a Square Chamber. *J Petrol Gas Chem Eng, 1*(1). 1-17.

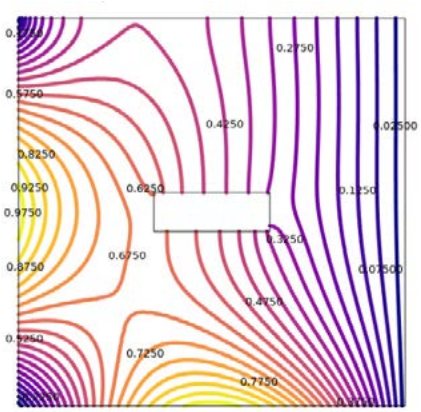

Figure 14: Isotherms Contour for *Ra* = 10^3

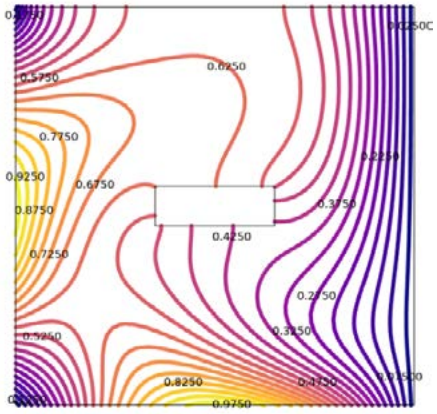

Figure 15: Isotherms Contour for *Ra* = 10^4

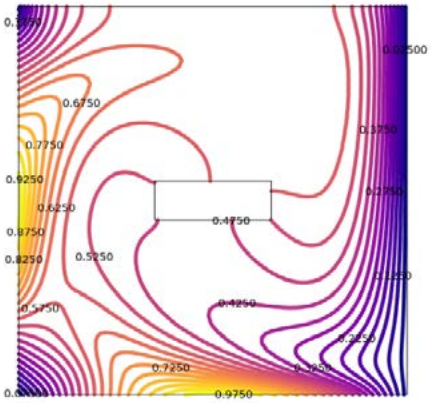

Figure 16: Isotherms Contour for *Ra* = 10^5

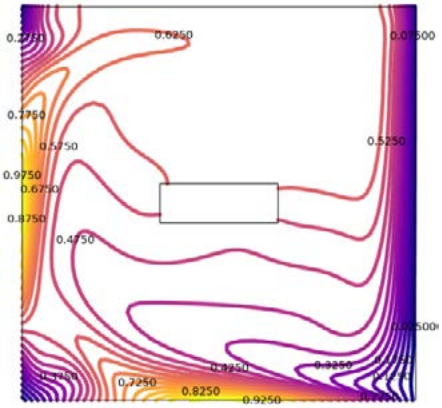

Figure 17: Isotherms Contour for *Ra* = 10^6

7.4 Effects of Rayleigh Number on Isotherm Contours (Heated Inner Wall)

The isotherm contours for various Rayleigh numbers (*Ra*) are shown in Figures 18 to 21, which show HT that shifts from being dominated by conduction to convection. The isotherms are comparatively smooth and parallel at lower Ra values (10^3 to 10^4, Figures 18 and 19), suggesting a substantial conduction effect. The isotherms become increasingly twisted and uneven when Ra rises to 10^5 to 10^6 (Figures 20 and 21), indicating the intensification of convective heat transmission. Stronger thermal convection effects are demonstrated by the tighter clustering of contours close to the heated borders at higher *Ra*, which emphasizes steeper temperature gradients. Around the heated and cooled surfaces, where buoyancy-driven flow creates thermal plumes, this effect is especially apparent. The incremental transition from a conduction-dominated environment to a convection-dominated one, where fluid motion greatly affects heat transfer efficiency, is highlighted by the growing intricacy of the isotherm patterns with greater *Ra*.

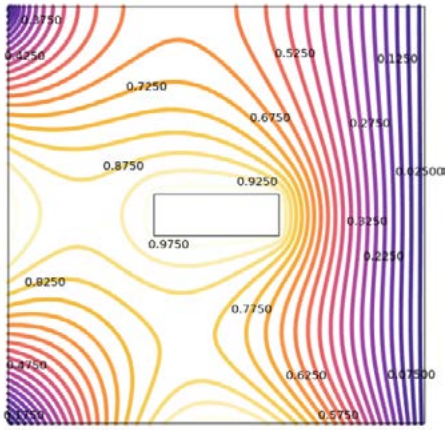

Figure 18: Isotherms Contour for *Ra* = 10^3

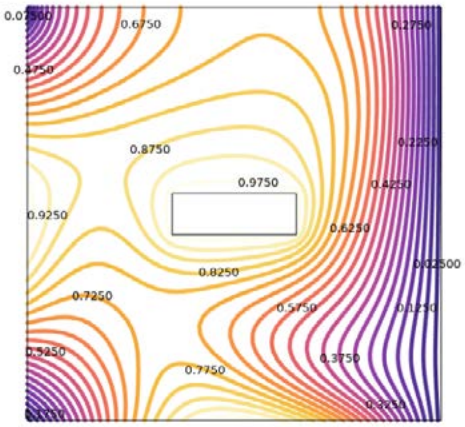

Figure 19: Isotherms Contour for *Ra* = 10^4

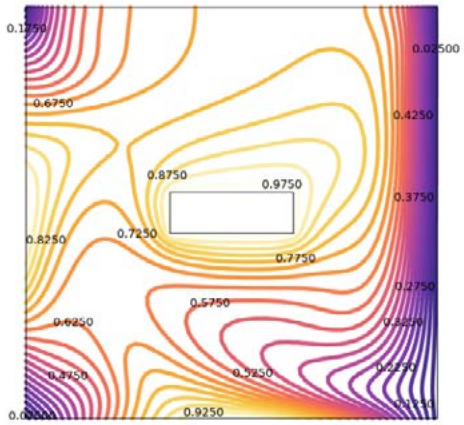

Figure 20: Isotherms Contour for $Ra = 10^5$

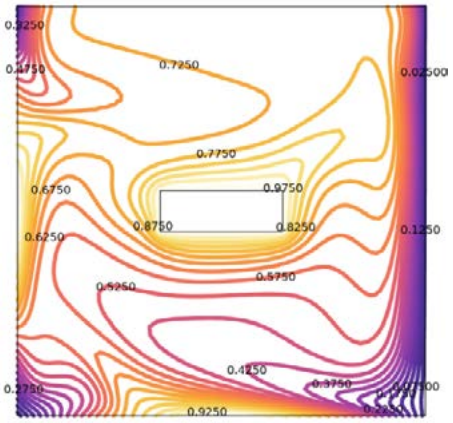

Figure 21: Isotherms Contour for $Ra = 10^6$

7.5 Effects of Rayleigh Number on Heat Transfer

7.5.1 Effect of Rayleigh Number on Nusselt Number Contour Plot (Non-Heated Inner Wall)

Nusselt number (*Nu*) contour plots are shown in Figures 22 to 25 for Rayleigh numbers (*Ra*) ranging from 10^3 to 10^6. The lowest Nu grows from 0.237 K/m to 0.343 K/m as *Ra* increases, while the maximum *Nu* increases from 9.13 K/m at $Ra = 10^3$ to 13.4 K/m at $Ra = 10^6$. Places with minimum heat transfer are indicated by green contours, whereas places with maximum heat transfer are indicated by red contours. Increased convective heat transport within the cavity is shown by more noticeable temperature gradients caused by higher *Ra*. Table 3 demonstrates that when *Ra* increases from 10^5 to 10^6, the minimum Nusselt value falls from 8.3446×10^{-4} K/m to 5.0934×10^{-5} K/m, indicating stronger convection and improved heat transfer. The maximum value increases from 10.538 K/m to 13.932 K/m.

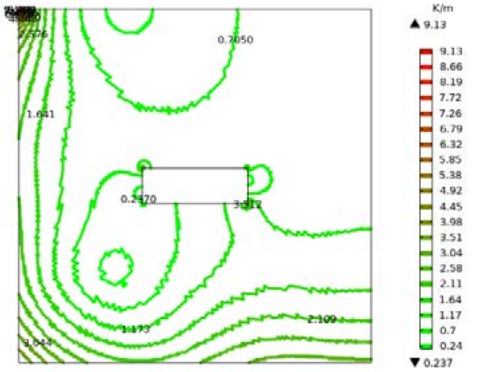

Figure 22: Nu Contour Plot for $Ra = 10^3$

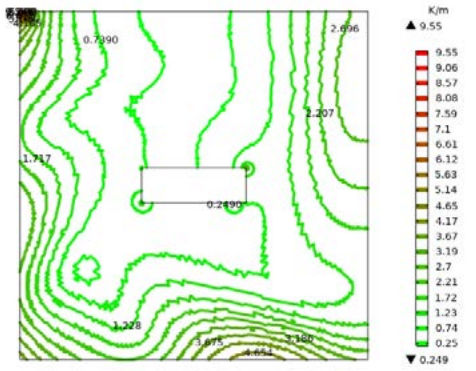

Figure 23: Nu Contour Plot for $Ra = 10^4$

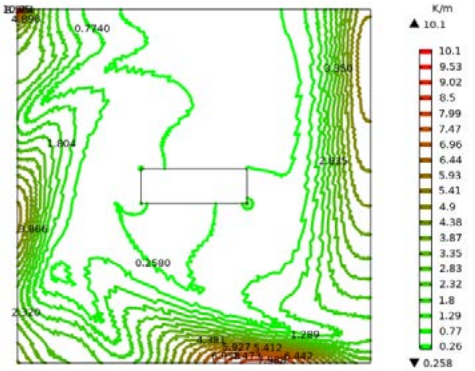

Figure 24: Nu Contour Plot for $Ra = 10^5$

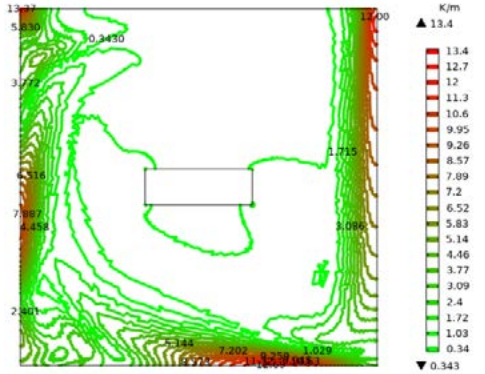

Figure 25: Nu Contour Plot for $Ra = 10^6$

Ra	Maximum value (K/m)	Minimum value (K/m)
10^5	10.538	8.3446E-4
10^6	13.932	5.0934E-5

Table 3: Nusselt Surface Maximum and Minimum Value for $Ra = 10^5$ and $Ra = 10^6$

7.5.2 Effect of Rayleigh Number on Nusselt Number Contour Plot (Heated Inner Wall)

The Nusselt number (*Nu*) contour plots for various Rayleigh numbers (*Ra*) are displayed in Figures 26 to 29, demonstrating the change in *HT* intensity. The contours are relatively uniform at lower *Ra* (10^3, 10^4), suggesting weaker convective effects. As *Ra* increases to 10^5 and 10^6, the contours become more irregular and concentrated around the heated surface, emphasizing enhanced convective heat transfer. The Nusselt surface values for *Ra* = 10^5 and *Ra* = 10^6 are shown in Table 4. The maximum values significantly increase with higher *Ra*, indicating stronger convection, while the minimum values remain very small, highlighting localized variations in heat transfer.

Ra	Maximum value (K/m)	Minimum value (K/m)
10^5	17.461	0.0015211
10^6	24.306	5.4109E-4

Table 4: Nusselt Surface Maximum and Minimum Value for *Ra* = 10^5 and *Ra* = 10^6

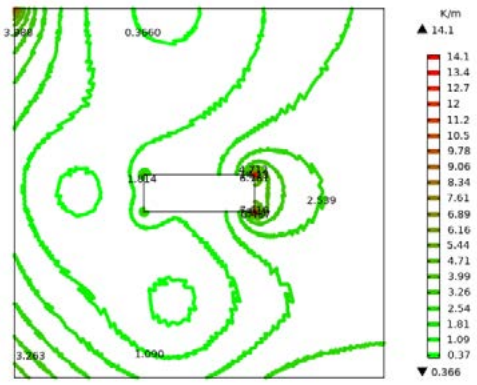

Figure 26: Nu Contour Plot for *Ra* = 10^3

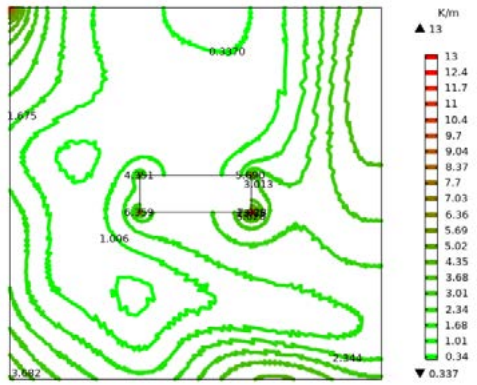

Figure 27: Nu Contour Plot for *Ra* = 10^4

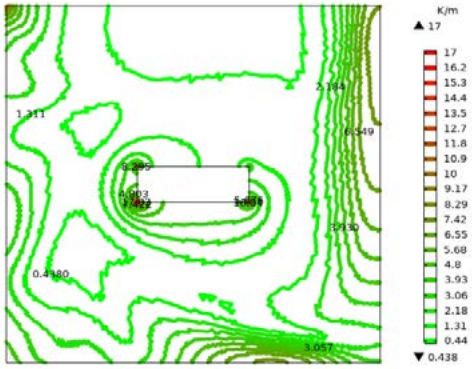

Figure 28: Nu Contour Plot for *Ra* = 10^5

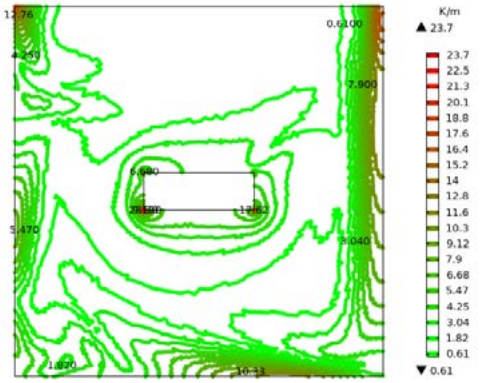

Figure 29: Nu Contour Plot for Ra = 10^6

7.5.3 Effects of Nusselt Number on Different Walls

The implications of the Nusselt number for various Rayleigh numbers (*Ra*) on the left, bottom, and the barriers on the other side are shown in Table 5. The table indicates improved convective heat transmission since the Nusselt number rises for all three sides when the Rayleigh number increases from 10^3 to 10^6. The bottom wall continuously has the greatest Nusselt number among the walls, followed by the left and right walls. The highest values of the Nusselt number for the left, bottom, and the barriers on the other side are 5.1889, 6.6084, and 10.177, respectively, for *Ra* = 10^6. According to this pattern, increased convection effects are a result of higher Rayleigh numbers, which enhance heat transmission across all surfaces.

Ra	Left wall	Bottom wall	Right wall	Inner-left wall	Inner-bottom wall	Inner-right wall	Inner top wall
10^3	2.5534	2.5774	2.2358	1.5769	1.8148	5.3176	2.0467
10^4	2.6886	3.2523	3.1776	2.2546	2.6686	3.9850	1.2403
10^5	3.1274	4.4613	5.8688	4.8296	4.0778	2.9250	1.7143
10^6	5.1889	6.6084	10.177	6.2169	5.7679	5.2330	3.0430

Table 5: Effects of Nusselt Number for Various Rayleigh Number on Different Wall

Effects of Nusselt Number for Different Rayleigh Number on Left Heated Wall

The Nusselt number's maximum and minimum values at the left heated wall for various Rayleigh numbers (*Ra*) are shown

in Table 6. The maximal Nusselt number likewise rises as *Ra* increases from 10^3 to 10^6, peaking at 17.475 for *Ra* = 106. Nonetheless, the minimum Nusselt number is comparatively low, ranging from 1.3102 to 1.5539, and does not exhibit a steady rising trend. The figure 30 also shows how the Nusselt number varies for various Rayleigh numbers along the arc length. The plot indicates increased convective heat transfer at the left heated wall, with higher *Ra* values producing more noticeable variations and peaks in the Nusselt number. This implies that fluctuations in local heat transfer become more noticeable as buoyancy-driven convection becomes stronger.

Ra	Maximum value	Minimum value
10^3	9.8035	1.3102
10^4	10.033	1.3612
10^5	10.753	1.5314
10^6	17.475	1.5539

Table 6: Maximum and Minimum Value of Nusselt Number at Left Vertical Heated Wall

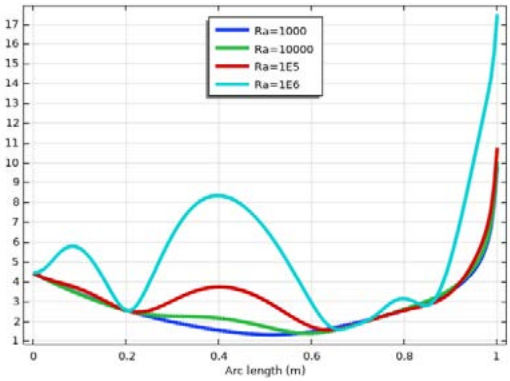

Figure 30: Effects of Nusselt Number for Different Rayleigh Numbers on the Left Heated Wall

Effects of Nusselt Number for Different Rayleigh Number on Bottom Heated Wall

The maximum and minimum values of the Nusselt number at the bottom heated wall for various Rayleigh numbers (*Ra*) are shown in Table 7. The maximum Nusselt number increases dramatically as *Ra* goes from 10^3 to 10^6, reaching 12.148 at *Ra* = 10^6, signifying improved convective heat transmission. The minimal Nusselt number, on the other hand, stays largely constant at 2.1. The change of the Nusselt number along the arc length for various *Ra* values is depicted in Figure 31, demonstrating that greater *Ra* results in more noticeable peaks and fluctuations. According to this pattern, rising *Ra* increases buoyancy-driven convection, which strengthens HT at the bottom barrier was heated.

Ra	Maximum value	Minimum value
10^3	4.4302	1.6052
10^4	4.4753	1.8707
10^5	7.5998	2.0402
10^6	12.148	2.0734

Table 7: Maximum and Minimum Value of Nusselt Number at Bottom Heated Wall

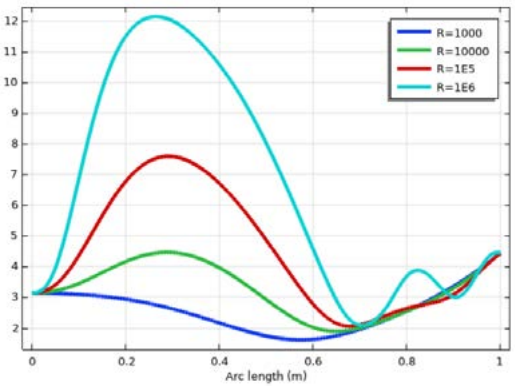

Figure 31: Effects of Nusselt Number for Different Rayleigh Number on Bottom Heated Wall

Effects of Nusselt Number for Different Rayleigh Number on Right Heated Wall

The maximum and minimum values of the Nusselt number at the right heated wall for various Rayleigh numbers (*Ra*) are shown in Table 8. The maximum Nusselt number rises significantly from 3.1332 to 16.868, whereas the lowest value climbs steadily from 1.8702 to 2.4233 as *Ra* grows from 10^3 to 10^6. Higher *Ra* values result in larger variations in heat transport, as seen by the variation of the Nusselt number throughout the arc length for various Rayleigh numbers in Figure 32. The plot indicates that the Nusselt number distribution becomes more dynamic as convection effects increase with increasing *Ra*. This is especially true at the beginning of the arc length, when a peak is shown before progressively declining and rising once more towards the finish.

Ra	Maximum value	Minimum value
10^3	3.1332	1.8702
10^4	4.4753	4.1867
10^5	7.9296	2.0598
10^6	16.868	2.4233

Table 8: Maximum and Minimum Value of Nusselt Number at Right Heated Wall

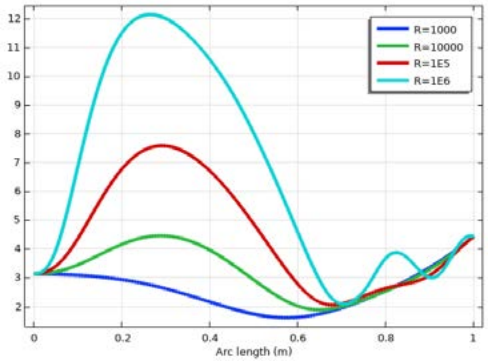

Figure 32: Effects of Nusselt Number for Different Rayleigh Number on Right Heated Wall

Effects of Nusselt Number for Different Rayleigh Number on Inner Left Wall

The upper and lower limits of the Nusselt number at the inner left wall for various Rayleigh numbers (*Ra*) are shown in Table 9. The maximum Nusselt number grows dramatically from 3.2451 to 15.606 as *Ra* goes from 10^3 to 10^6, and the minimum value likewise increases from 1.2154 to 4.3460. The Nusselt number fluctuation over the arc length for various Ra values is depicted in Figure 33, which demonstrates that greater *Ra* results in improved heat transmission and more noticeable Nusselt number variations. The plot shows that the Nusselt number is rather constant for lower *Ra*, but it rises more sharply towards the end of the arc length at higher *Ra*, indicating stronger convection effects close to the borders.

Ra	Maximum value	Minimum value
10^3	3.2451	1.2154
10^4	5.2118	1.7370
10^5	11.103	3.7397
10^6	15.606	4.3460

Table 9: Maximum and Minimum Value of Nusselt Number at Inner Left Wall

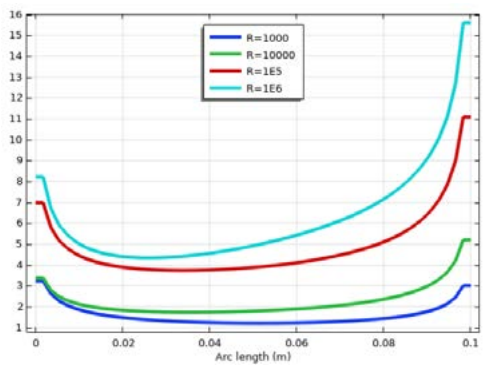

Figure 33: Effects of Nusselt Number for Different Rayleigh Number on Inner Left Wall

Citation: Rahman, A., Islam, S., Parven, R., Hossain, A. (2024). Computational Analysis of the Impacts of Inner Obstacles and Periodic Heating on Heat Transfer for Natural Convection Fluid Flow Inside a Square Chamber. *J Petrol Gas Chem Eng, 1*(1). 1-17.

Effects of Nusselt Number for Different Rayleigh Number on Inner Bottom Wall

The inner bottom wall's maximum and minimum Nusselt number values for various Rayleigh numbers (*Ra*) are shown in Table 10. According to the statistics, both the maximum and minimum Nusselt numbers rise as *Ra* increases from 10^3 to 10^6. The lowest values range from 1.1019 to 4.8191, while the largest values range from 8.5857 to 15.457. At greater *Ra*, this pattern indicates improved convective heat transmission. The consequences of the Nusselt number fluctuation along the inner bottom wall for various Rayleigh numbers are further depicted in Figure 34, which displays a lower, comparatively stable zone in the middle and a notable increase along the borders. The trend seen in Table 8 is further supported by the graph, which illustrates the effect of increasing *Ra*. Higher values result in more fluctuations in the Nusselt number distribution.

Ra	Maximum value	Minimum value
10^3	8.5857	1.1019
10^4	8.4882	2.0436
10^5	11.235	3.3694
10^6	15.457	4.8191

Table 10: Maximum and Minimum Value of Nusselt Number at Inner Bottom Wall

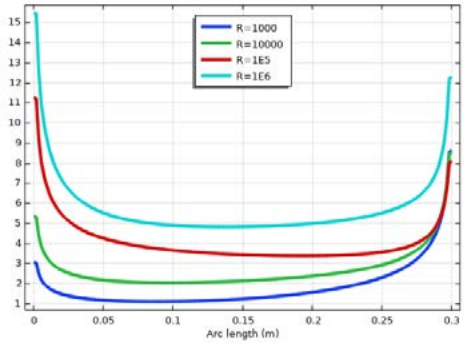

Figure 34: Effects of Nusselt Number for Different Rayleigh Number on Inner Bottom Wall

Effects of Nusselt Number for Different Rayleigh Number on Inner Right Wall

The inner right wall's maximum and minimum Nusselt number values for various Rayleigh numbers (*Ra*) are shown in Table 11. The highest Nusselt number first falls from 9.4506 at 10^3 *Ra* to 7.7575 at 10^5 *Ra*, before increasing once again to 11.971 at 10^6 Ra, indicating a nonmonotonic trend in the data. The lowest values follow a similar pattern, decreasing from 4.4239 at 10^3 *Ra* to 2.0516 at 10^5 *Ra* before rising to 4.0573 at 10^6 *Ra*. The variation of the Nusselt number along the inner right wall for various Rayleigh numbers is shown in Figure 35. It shows a declining trend from the top, followed by a rise close to the bottom of the wall. The complicated nature of convective heat transport on the right wall is reflected in the curves, which show that fluctuations in the Nusselt number become increasingly noticeable at greater *Ra*.

Ra	Maximum value	Minimum value
10^3	9.4506	4.4239
10^4	8.6421	3.1903
10^5	7.7575	2.0516
10^6	11.971	4.0573

Table 11: Maximum and Minimum Value of Nusselt Number at Inner Right Wall

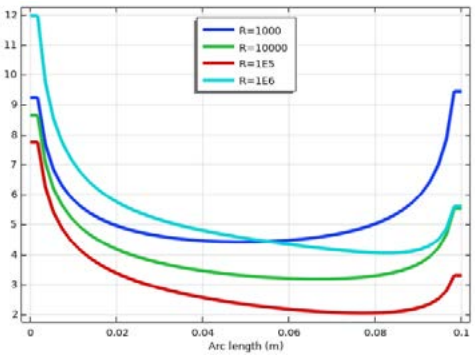

Figure 35: Effects of Nusselt Number for Different Rayleigh Number on Inner Right Wall

Citation: Rahman, A., Islam, S., Parven, R., Hossain, A. (2024). Computational Analysis of the Impacts of Inner Obstacles and Periodic Heating on Heat Transfer for Natural Convection Fluid Flow Inside a Square Chamber. *J Petrol Gas Chem Eng, 1*(1). 1-17.

Effects of Nusselt Number for Different Rayleigh Number on Inner Top Wall

The inner top wall's maximum and minimum Nusselt number values for various Rayleigh numbers (*Ra*) are shown in Table 12. With the highest Nusselt number falling from 8.9538 at 10^3 *Ra* to 4.9808 at 10^4 *Ra*, then climbing to 6.5516 at 10^5 *Ra* and then rising to 8.3402 at 10^6 *Ra*, the data display a fluctuating trend. The minimum values follow a similar pattern, first declining from 1.3542 at 10^3 *Ra* to 0.8707 at 10^4 *Ra* then progressively increasing to 2.1445 at 10^6 *Ra*. The effects of varying Rayleigh numbers on the Nusselt number along the inner top wall are shown in Figure 36. The graph highlights the impact of buoyancy-driven convection on heat transmission by showing a notable drop in the middle part and an increase at the edges. More dynamic thermal activity along the top wall is shown by the changes at greater *Ra*.

Ra	Maximum value	Minimum value
10^3	8.9538	1.3542
10^4	4.9808	0.8707
10^5	6.5516	1.1885
10^6	8.3402	2.1445

Table 12: Maximum and Minimum Value of Nusselt Number at Inner Top Wall

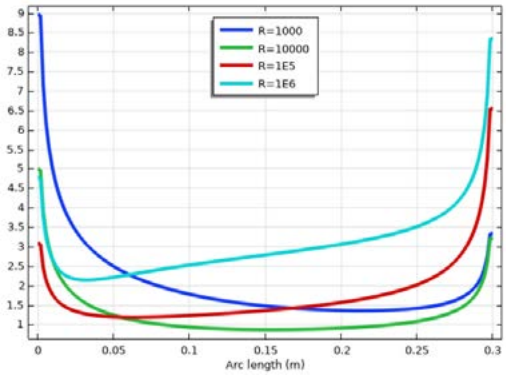

Figure 36: Effects of Nusselt Number for Different Rayleigh Number on Inner Top Wall

Effects of Nusselt Number for Different Rayleigh Number on Velocity Magnitude

The maximum and minimum velocity magnitude values for various Rayleigh numbers (*Ra*) are displayed in Table 13, which also demonstrates an increasing trend in the maximum velocity magnitude as *Ra* rises. In particular, the greatest velocity for *Ra* = 10^3 is 2.7714 m/s, and for *Ra* = 10^6, it reaches 276.19 m/s. The minimum value stays at 0.0000 in all circumstances. Figure 37, which shows the velocity magnitude variation over the arc length for various Rayleigh numbers, provides additional evidence of this trend. Higher *Ra* values result in a noticeable increase in velocity on the graph, with more prominent peaks signifying stronger convective motion.

Ra	Maximum value	Minimum value
10^3	2.7714	0.0000
10^4	22.218	0.0000
10^5	90.299	0.0000
10^6	276.19	0.0000

Table 13: Maximum and Minimum Value of Velocity Magnitude

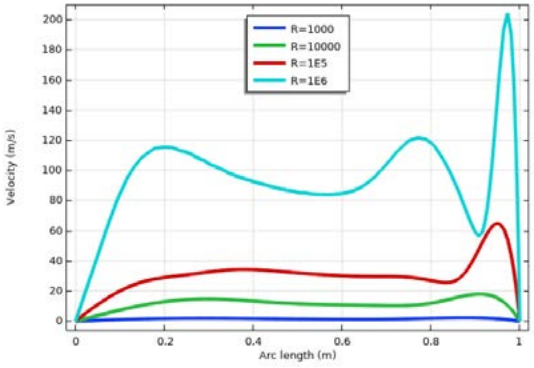

Figure 37: Velocity Magnitude

7.6 Effects of Average Nusselt Number on Non-Heated Inner Wall and Heated Inner Wall

The relationship between the Nu_{av} and the *Ra* for various wall layouts in a heated enclosure is depicted in Figures 38 and 39. The results for the left wall (LW) are shown in Figure 38, which contrasts examples with a heated inner wall (HIW) and a non-heated inner wall (NHIW). The heated inner wall (LW-HIW) continuously displays higher values than the non-heated inner wall (LW-NHIW), demonstrating that the Nu_{av} grows as the *Ra* does. The fluctuation of the Nusselt number for the bottom wall (BW) under the identical circumstances is also shown in Figure 39. In this instance as well, more convective HT occurs when heating is present because the heated inner wall (BW-HIW) has a higher Nusselt number than the non-heated inner wall (BW-NHIW). According to the patterns in both images, heat transfer becomes more intense as the Rayleigh number rises, and the heated inner wall plays a major role in this improvement.

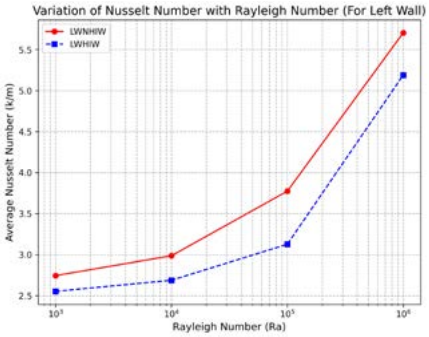

Figure 38: Average Nusselt Number in Left Wall (Lw) for Non-Heated Inner Wall (NHIW) and Heated Inner Wall (HIW)

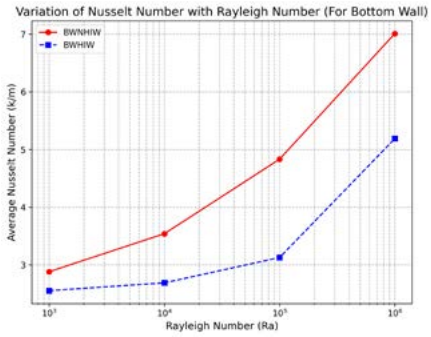

Figure 39: Average Nusselt Number in Bottom Wall (BW) for Non-Heated Inner Wall (NHIW) and Heated Inner Wall (HIW)

8. Conclusion

Effect of Rayleigh Number on Heat Transfer: Greater temperature gradients and N indicate that convective heat transport and HT within the cavity intensify as the *Ra* rises.

Isotherm Contour: Stronger convective effects and better heat transport are indicated by more irregular isotherm contours, which are more common at $Ra = 10^6$.

Nusselt Number (Nu) for Non-Heated Inner Wall: As *Ra* increases, the Nusselt number rises as well, reaching a high of 13.4 K/m at $Ra = 10^6$ from 9.13 K/m at $Ra = 10^3$, indicating improved heat transfer and stronger convection.

Heated Inner Wall Nusselt Number (Nu): As in the non-heated case, the Nusselt number rises with *Ra*, reaching its highest values at 17.461 K/m at $Ra = 10^5$ and 24.306 K/m at $Ra = 10^6$.

Impact of Rayleigh Number on Various Walls: As *Ra* rises, the Nusselt number rises for every wall. The Nusselt number is continuously highest on the bottom wall, followed by the left and right walls.

Maximum and Minimum Nu for Particular Walls: For the heated walls (left, bottom, and right), the minimum values of Nusselt numbers stay low, showing localized heat transmission differences, while the maximum values dramatically rise with *Ra*, suggesting higher convective heat transfer.

Velocity Magnitude: Stronger convective motion is indicated by a significant increase in the maximum velocity magnitude with Ra. At $Ra = 10^6$, the maximum velocity recorded is 276.19 m/s.

Average Nusselt Number: When there is a contentious inner wall (HIW), heat transfer is stronger when the Nuav rises with the *Ra*. The heated inner wall continuously produces greater Nusselt numbers than the non-heated inner wall (NHIW) in both the left wall (LW) and bottom wall (BW). This demonstrates that when Rayleigh numbers increase, heating improves convective heat transfer.

In decision: Stronger fluid motion, larger temperature gradients, and higher Nusselt numbers are the results of enhanced convective heat transfer caused by higher Rayleigh numbers. The bottom wall has the largest Nusselt value, indicating that heated walls transfer heat most efficiently.

9. References

1. Maravedi, S. M., & Farhadi, F. (2016). Natural convection in circular enclosures heated from below for various central angles. *Case Studies in Thermal Engineering, 8*, 322-329.
2. Al-Rashed, A. A., Kolsi, L., Hussein, A. K., Hassen, W., Aichouni, M., & Borjini, M. N. (2017). Numerical study of three-dimensional natural convection and entropy generation in a cubical cavity with partially active vertical walls. *Case Studies in Thermal Engineering, 10*, 100-110.
3. Wiriyasart, S., & Naphon, P. (2020). Thermal management system with different configuration liquid vapor chambers for high power electronic devices. *Case Studies in Thermal Engineering, 18*, 100590.
4. Haghighi, A., Albojamal, A., & Vafai, K. (2020). Heat removal enhancement in a channel with a single or an array of metallic foam obstacles. *International Journal of Thermal Sciences, 149,* 106057.
5. Mezrhab, A., Jami, M., Abid, C., Bouzidi, M. H., &

Lallemand, P. (2006). Lattice-Boltzmann modelling of natural convection in an inclined square enclosure with partitions attached to its cold wall. *International journal of heat and fluid flow, 27*(3), 456-465.
6. Yu, Z. T., Xu, X., Hu, Y. C., Fan, L. W., & Cen, K. F. (2011). Unsteady natural convection heat transfer from a heated horizontal circular cylinder to its air-filled coaxial triangular enclosure. *International Journal of Heat and Mass Transfer, 54*(7-8), 1563-1571.
7. Khatamifar, M., Lin, W., & Dong, L. (2021). Transient conjugate natural convection heat transfer in a differentially-heated square cavity with a partition of finite thickness and thermal conductivity. *Case Studies in Thermal Engineering, 25*, 100952.
8. Han, X., Meng, X., & Li, C. (2015). Buoyancy-driven convection heat transfer of copper–water nanofluid in a square enclosure under the different periodic oscillating boundary temperature waves. *Case Studies in Thermal Engineering, 6*, 93-103.
9. Dogonchi, A. S., Seyyedi, S. M., Hashemi-Tilehnoee, M., Chamkha, A. J., & Ganji, D. D. (2019). Investigation of natural convection of magnetic nanofluid in an enclosure with a porous medium considering Brownian motion. *Case Studies in Thermal Engineering, 14*, 100502.
10. Yu, P. X., Qiu, J. X., Qin, Q., & Tian, Z. F. (2013). Numerical investigation of natural convection in a rectangular cavity under different directions of uniform magnetic field. *International Journal of Heat and Mass Transfer, 67*, 1131-1144.
11. Ghasemi, B., Aminossadati, S. M., & Raisi, A. (2011). Magnetic field effect on natural convection in a nanofluid-filled square enclosure. *International Journal of Thermal Sciences, 50*(9), 1748-1756.
12. Oreper, G. M., & Szekely, J. (1983). The effect of an externally imposed magnetic field on buoyancy driven flow in a rectangular cavity. *Journal of Crystal Growth, 64*(3), 505-515.
13. Garandet, J. P., Alboussiere, T., & Moreau, R. (1992). Buoyancy driven convection in a rectangular enclosure with a transverse magnetic field. *International journal of heat and mass transfer, 35*(4), 741-748.
14. Rudraiah, N., Barron, R. M., Venkatachalappa, M., & Subbaraya, C. K. (1995). Effect of a magnetic field on free convection in a rectangular enclosure. *International Journal of Engineering Science, 33*(8), 1075-1084.
15. Geridonmez, B. P., & Oztop, H. F. (2020). Natural convection in a cavity under partial magnetic field applied from different corners. *International Communications in Heat and Mass Transfer, 114,* 104575.
16. Son, J. H., & Park, I. S. (2017). Numerical study of MHD natural convection in a rectangular enclosure with an insulated block. *Numerical Heat Transfer, Part A: Applications, 71*(10), 1004-1022.
17. Hossain, M. S., & Alim, M. A. (2014). MHD free convection within trapezoidal cavity with non-uniformly heated bottom wall. *International Journal of Heat and Mass Transfer, 69*, 327-336.
18. Sivasankaran, S., & Ho, C. J. (2008). Effect of temperature dependent properties on MHD convection of water near its density maximum in a square cavity. *International Journal of Thermal Sciences, 47*(9), 1184-1194.
19. Ece, M. C., & Büyük, E. (2006). Natural-convection flow under a magnetic field in an inclined rectangular enclosure heated and cooled on adjacent walls. *Fluid dynamics research, 38*(8), 564.
20. Singh, R. J., & Gohil, T. B. (2019). The numerical analysis on the development of Lorentz force and its directional effect on the suppression of buoyancy-driven flow and heat transfer using OpenFOAM. *Computers & Fluids, 179,* 476-489.
21. Singh, R. J., & Gohil, T. B. (2019). The numerical analysis on the variation of electric potential, electric current and Lorentz force with its influence on buoyancy-driven conjugate heat transfer and fluid flow using OpenFOAM. *Fusion Engineering and Design, 148*, 111300.
22. Ramonu, O. J., Afolabi, S. I., & Akinyemi, T. O. (2018). Natural convection of air in a rectangular cavity with partially heated and cooled side walls.
23. Parvin, S., & Nasrin, R. (2011). Analysis of the flow and heat transfer characteristics for MHD free convection in an enclosure with a heated obstacle. *Nonlinear Analysis: Modelling and Control, 16*(1), 89-99.
24. Chowdhury, R., Khan, M. A. H., & Siddiki, M. N. A. A. (2015). Natural convection in porous triangular enclosure with a circular obstacle in presence of heat generation. *American Journal of Applied Mathematics, 3*(2), 51-58.
25. House, J. M., Beckermann, C., & Smith, T. F. (1990). Effect of a centered conducting body on natural convection heat transfer in an enclosure. *Numerical Heat Transfer, 18*(2), 213-225.
26. Kandaswamy, P., Lee, J., & Hakeem, A. A. (2007). Natural convection in a square cavity in the presence of heated plate. *Nonlinear Analysis: Modelling and Control, 12*(2), 203-212.
27. Mousa, M. M. (2016). Modeling of laminar buoyancy convection in a square cavity containing an obstacle. *Bulletin of the Malaysian Mathematical Sciences Society, 39,* 483-498.
28. Rahman, M. M., Alim, M. A., Saha, S., & Chowdhury, M. K. (2008). A numerical study of mixed convection in a square cavity with a heat conducting square cylinder at different locations. *Journal of Mechanical Engineering, 39*(2), 78-85.
29. Saleh, H., Roslan, R., & Hashim, I. (2011). Natural convection heat transfer in a nanofluid-filled trapezoidal enclosure. *International journal of heat and mass transfer, 54*(1-3), 194-201.
30. Uddin, H., Saha, S., & Hasan, M. N. (2008). Natural convection flows in a trapezoidal enclosure with isoflux heating from below. *Proceedings of the 12th Annual Paper Meet, 8,* 9.
31. Roy, S., & Basak, T. (2005). Finite element analysis of natural convection flows in a square cavity with non-uniformly heated wall (s). *International Journal of Engineering Science, 43*(8-9), 668-680.
32. Billah, M. M., Rahman, M. M., Saidur, R., & Hasanuzzaman, M. (2011). Simulation of MHD mixed convection heat transfer enhancement in a double lid-driven obstructed enclosure. *International Journal of Mechanical and Materials Engineering, 6*(1), 18-30.

33. Oztop, H. F., Al-Salem, K., & Pop, I. (2011). MHD mixed convection in a lid-driven cavity with corner heater. *International Journal of Heat and Mass Transfer, 54*(15-16), 3494-3504.
34. Basak, T., Pradeep, P. K., Roy, S., & Pop, I. (2011). Finite element based heatline approach to study mixed convection in a porous square cavity with various wall thermal boundary conditions. *International Journal of heat and mass transfer, 54*(9-10), 1706-1727.
35. Nasrin, R. (2011). Mixed magnetoconvection in a lid-driven cavity with a sinusoidal wavy wall and a central heat conducting body. *Journal of Naval Architecture and Marine Engineering, 8*(1), 13-24.
36. Kabir, K. H., Alim, M. A., & Andallah, L. S. (2013). Effects of viscous dissipation on MHD natural convection flow along a vertical wavy surface. *Journal of Theoretical and Applied Physics, 7,* 1-8
37. Hossain, M. A., Sajib, M. A. H., Sagib, M., Islam, M. R., Barai, G., Podder, C., & Saha, B. K. (2025). Enhanced thermal efficiency on mixed convection flow of TiO2–Water nanofluid inside a double lid driven zigzag cavity with and without heated obstacles insertion. *International Journal of Thermofluids, 25,* 101040
38. Mahmuda Maya, M. U., Alam, M. N., & Refaie Ali, A. (2023). Influence of magnetic field on MHD mixed convection in lid-driven cavity with heated wavy bottom surface. *Scientific Reports, 13*(1), 18959
39. Zienkiewicz, O. C., & Taylor, I. R. L. (1991). The Finite Element Method 4th edition McGraw-Hill

Nomen Clature

L Length of the Square Cavity
l Length of the Rectangular Block
H Height of the Rectangular Block
T_h Heated Wall Temperature
T_c Cold Wall Temperature
T Temperature
u, v Dimensionless Velocity Coordinates
P_r Prandtl Number
R_a Rayleigh Number
K Thermal Conductivity
C_p Specific Heat
B_f Body Force
γ Ratio of Specific Heat
P Dimensionless Pressure

Greek Symbols

α Coefficient of Thermal Diffusivity, $m^2 s^{-1}$
ρ Density of Fluid, kg m^{-3}
θ Dimensionless Temperature
μ Dynamic Viscosity, kg m^{-1} s^{-1}

Subscripts

c Cool
h Hot